Corrosion Science 240 (2024) 112496

Contents lists available at ScienceDirect

Corrosion Science

journal homepage: www.elsevier.com/locate/corsci

Understanding preferential intergranular oxidation in alloy X-750 in 480 °C CO-CO_2 environments at the nanoscale

A.E. Yaedu [a], L. Volpe [b], A. Shaik [a], F. Long [a], K. Daub [a], F. Scenini [c], S.Y. Persaud [a,*]

[a] Department of Mechanical and Materials Engineering, Queen's University, 60 Union Street W, Kingston, ON K7L 2N8, Canada
[b] Material Division, Culham Campus, United Kingdom Atomic Energy Authority, Abingdon OX14 3DB, United Kingdom
[c] Department of Materials, The University of Manchester, Oxford Road, Manchester M13 9PL, United Kingdom

ARTICLE INFO

Keywords:
Alloy X-750
PWSCC
Preferential intergranular oxidation
CANDU nuclear power systems

ABSTRACT

Alloy X-750 was exposed to a 480 °C CO-CO_2 reducing gas mixture at an oxygen partial pressure below the NiO dissociation pressure. Post-exposure analytical transmission electron microscopy (ATEM) analysis confirmed the occurrence of preferential intergranular oxidation (PIO) and internal oxidation which resulted in the formation of Ni nodules. Thus, reducing CO-CO_2 mixtures can promote PIO in Alloy X-750, similar to Alloy 600 exposed to similar oxygen partial pressure but in H_2-steam environment. In Alloy X-750, intergranular oxidation of Ti and Al were observed to occur prior to Cr oxidation, while the presence of intergranular Cr carbides hinders PIO penetration depth.

1. Introduction

Alloy X-750 is a Ni-based, precipitation-hardened alloy containing Al and Ti which produce γ' Ni_3(Ti, Al) precipitates [1,2]. In nuclear power plants, it is employed for components such as bolts, springs, beams, and guide tube pins [3,4]. Both Alloy X-750 and its parent variant, Alloy 600 (Ni-16Cr-9Fe), are susceptible to primary water stress corrosion cracking (PWSCC). In Canada Deuterium Uranium (CANDU) Reactors, primary water conditions consist of a temperature between 267 and 312 °C and pH_a between 10.2 and 10.4 (apparent pH of a heavy water solution measured with traditional light water pH electrodes), measured at 25 °C, controlled with lithium hydroxide; furthermore, 3–10 ml/kg H_2/H_2O is added to prevent net decomposition of water by radiolysis [5,6]. The susceptibility of both alloys to PWSCC was originally reported by Coriou et al.; first in Alloy 600 [7] and later in Alloy X-750 [8]. Cracked support pins manufactured in Alloy X-750 were identified during refueling of Mihama 3, Japan in 1978 [9], becoming the first observed occurrence of PWSCC in Alloy X-750. Similar problems were reported the following year in France and the USA [10]. Noting that the components supplied with a dissimilar heat treatment on the same reactor had no cracks, numerous heat treatments were tested aiming to improve the PWSCC resistance [9,11,12]. The HTH treatment (high temperature heat-treatment [13]), which consists in annealing at 1093 °C for 1 h followed by water quenching and aging at 704 °C for 20 h resulted in a microstructure most resistant to PWSCC, albeit not imparting immunity [14–17]. This heat treatment results in formation of a semi-continuous distribution of intergranular carbides, which has been shown to play a crucial role in increasing PWSCC resistance [3,11,12,18].

In CANDU reactors, garter-spring spacers are placed between pressure tubes and calandria tubes to separate and maintain a dry CO_2-O_2 insulating gas gap [19]. The annulus gas system (AGS) where spacers reside is, in normal conditions, an oxidizing dry gas environment due to the addition of 0.5–5 vol% O_2, with the dew point constantly monitored to detect moisture [19]. The system is purged when the dew point is above −10 °C, ruling out any possibility of aqueous-based SCC. As the Zr-2.5 Nb pressure tubes experience irradiation creep over time [6], spacers maintain a gap, preventing contact between the calandria and pressure tubes, which otherwise could result in formation of brittle zirconium hydrides in pressure tubes, leading to cracking [19]. As a consequence of pressure tube creep, the spacers are "pinched" between the pressure and calandria tubes, leading to differential temperatures around their circumference. It is estimated that at the 6 o'clock position the temperature ranges between 120 and 280 °C and at the 12 o'clock position the temperature ranges between 300 and 330 °C [20].

Spacers are made of either Alloy X-750 or Zr-based alloys [19,21]. X-750 spacers are hot coiled from 0.76 by 0.76 mm cross-section square wire followed by HTH heat treatment [6,22]. Crush tests revealed that Alloy X-750 spacer material is susceptible to embrittlement in the AGS

* Corresponding author.
E-mail addresses: 19aey@queensu.ca (A.E. Yaedu), suraj.persaud@queensu.ca (S.Y. Persaud).

https://doi.org/10.1016/j.corsci.2024.112496
Received 7 July 2024; Received in revised form 16 September 2024; Accepted 30 September 2024
Available online 1 October 2024

environment [21,23]. Specifically, they are exposed to a high thermal neutron flux which results in significant Ni transmutation, producing H and He, along with γ' disordering and dissolution [20,24,25]. Thus, irradiation embrittlement is attributed to the formation of cavities stabilized by He that tend to segregate at higher density at grain boundaries and matrix-precipitate interfaces [24,26,27]. Although irradiation is a known source of Alloy X-750 spacer embrittlement, any contribution from the AGS environment has not been studied, especially for crack initiation. Since Alloy X-750 is susceptible to PWSCC in reactor coolant environments, similar embrittlement and crack initiation from dry CO/CO_2 gas environments may be relevant in the AGS if the oxygen partial pressure is below (or near) the NiO dissociation pressure as it is the case for Alloy 600. While such reducing conditions are not likely in the AGS, which is normally oxidizing, understanding the behaviour of Alloy X-750 in rare off-chemistry conditions is still useful. In such a hypothetical event, the absence of oxygen and ingress of deuterium leads to the reduction of CO_2 to CO.

It is believed that PWSCC is governed by an oxidation-based mechanism where the Cr concentration is important. Among the various proposed models for PWSCC of Alloy 600, the internal oxidation model, first proposed by Scott and Le Calvar [28], is often cited as viable. This model suggests that PWSCC is associated with an internal oxidation mechanism due to conditions of primary water being in the vicinity of the Ni/NiO equilibrium electrode potential. The model has evolved since its initial proposal to the currently most accepted preferential intergranular oxidation (PIO) model [29–34]. Several studies have reported that the maximum PWSCC susceptibility for Alloys 600 and X-750 occurs at a potential near the Ni/NiO equilibrium electrode potential, where Ni-metal is thermodynamically stable [35,36], even though Ni containing oxide spinels ($NiFe_2O_4$ and $NiCr_2O_4$) may form at lower oxygen partial pressures [37,38]. These electrochemical conditions, combined with the fact that Alloys 600 and X-750 have relatively low Cr content (~16 wt%), results in inward oxide growth along grain boundaries rather than external oxide formation [39,40]. This PIO leads to intergranular embrittlement and PWSCC. A high-temperature (480 °C), low-pressure H_2-steam environment has been used to simulate accelerated primary water conditions for laboratory testing of Alloy 600 [29–31,41–44]. Usually, the oxygen partial pressure is maintained below the NiO equilibrium dissociation pressure [45,46], resulting in PIO of the reactive elements, particularly Cr, Al, and Ti. Similar to 300 °C primary water, lattice diffusion is negligible in 480 °C hydrogenated steam leading to grain boundary oxidation phenomena being dominant [47]. Additionally, diffusion-induced grain boundary migration (DIGM) and the formation of Ni nodules on the surface are commonly observed in Alloy 600 exposed to 480 °C hydrogenated steam. The formation of Ni nodules are due to relieving of compressive stress resulting from internal oxidation [48,49].

A recent study in X-750 [50] showed that reducing 480 °C CO-CO_2 mixtures can promote both internal and intergranular oxidation similar to observations in Alloy 600 exposed to 480 °C H_2-steam. The aim of this work is to further examine this internal and intergranular oxidation using analytical transmission electron microscopy (ATEM) methods to provide mechanistic insight. This accelerated CO-CO_2 environment allows for initial evaluation of intergranular oxidation in Alloy X-750 where the oxygen partial pressure is below the Ni/NiO dissociation pressure, resulting in PIO. It should be re-emphasized that such a reducing environment has not been reported in the AGS of CANDU reactors at present. This is a proactive study aiming to determine the thermodynamic and kinetic boundary conditions for the occurrence of PIO in the AGS, from which a future transient or off-chemistry environment could be compared to. Annealed and aged (HTH) Alloy X-750 samples were tested in environments where the oxygen partial pressure is maintained at 500× and 5000× below the NiO equilibrium dissociation pressure. Post-exposure characterization is performed using scanning electron microscopy (SEM) and analytical transmission electron microscopy (ATEM) techniques, with emphasis on identifying PIO and the effect of heat treatment.

2. Experimental methods

2.1. Material and sample preparation

The Alloy X-750 plate used in this study was provided by Haynes International (Heat n° 275097671) with a nominal thickness of 1.09 mm. This material was supplied as cold rolled and annealed with a chemical composition shown in Table 1. Prior to oxidation experiments, the material was heat-treated following the HTH procedure: Solution annealing was conducted in high-purity argon gas for one hour at 1093 ± 5 °C and water quenched within 10 s, thermal aging was performed at 704 ± 5 °C in argon gas for 20 h and air cooled. However, unlike the spacers, the samples were not cold or hot worked before heat treatment. Square coupons of 7 mm × 7 mm in area were cut and ground with SiC paper to a 1000 grit finish, followed by sequential polishing with diamond suspension (6 μm, 3 μm, and 1 μm). The final polishing step was performed using colloidal silica (60 nm) to remove any deformation induced by mechanical polishing, because the removal of the ultrafine-grained layer associated with grinding and polishing can have significant effects on oxide formation and can obscure mechanistic understanding [51,52]. After polishing, the samples were ultrasonically cleaned in acetone and ethanol for 10 min each, rinsed with de-ionized water, and dried with nitrogen gas.

2.2. Gas testing

The polished samples were tested in a gas reactor rig, which allows for the exposure of samples to CO-CO_2 gas mixtures at elevated temperatures to simulate extreme off-chemistry AGS conditions, Fig. 1. This low pressure experiment rig is operated near atmospheric pressure and is similar to the system developed by Scenini et al. [53], where the gas mixture is pre-heated in the annular space of a specially designed double-walled quartz tube before entering the inner tube and coming in contact with the samples. By controlling the ratio of CO and CO_2, the oxygen partial pressure can be set relative to the NiO oxygen dissociation pressure using thermodynamic calculations. Using the approach stated in the literature [46], the equilibrium oxygen partial pressure (p_{O_2}) was calculated using the Gibbs free energy, Eq. (1). At 480 °C, the Gibbs free energy was calculated to be −170.9 kJ/mol, resulting in the equilibrium p_{O_2} being 1.98×10^{-24} bar.

$$p_{O_2} = \left[\exp\left(\frac{\Delta G^{\circ}_{f,NiO}}{RT}\right)\right]^2 \quad (1)$$

Tests in mixed gas environments were all conducted at 480 °C for 192 h. Duplicate testing at each environment condition was performed to ensure consistent results. In each experiment, one annealed and one thermally aged sample were exposed simultaneously. During service the γ' precipitates in Alloy X-750 are disordered and dissolved over time due to irradiation [24]. Since aging promotes the precipitation of intergranular carbides and the γ' secondary phase, testing annealed and thermally aged samples allows for comparing Alloy X-750 prior to (aged samples) and after (annealed samples) dissolution of γ' to simulate the effect of irradiation.

The p_{O_2} in the experimental environment is determined by the CO/CO_2 gas equilibrium and calculated using Eq. (2), and assuming $\Delta G_{f,CO_2} = -218.35$ kJ/mol. Setting p_{O_2} equivalent to the Ni/NiO equilibrium oxygen partial pressure, the ratio of CO to CO_2 was found to be 2463:1; a lower ratio results in a more reducing environment, where Ni is not oxidized to NiO. Varying the ratio of CO and CO_2 allows for setting the desired environment relative to the Ni/NiO equilibrium, in this study defined as the number of times below the NiO oxygen dissociation pressure. The oxygen partial pressure was set to 500 and 5000 times below the NiO dissociation pressure (designated from now on as 500×

Table 1
The chemical composition (in wt%) for the Alloy X-750 material used in this study, provided by the supplier.

Ni	Cr	Fe	Ti	Nb	Al	Si	Mn	C	Cu
71.83	15.42	8.25	2.45	0.96	0.68	0.23	0.21	0.05	0.01

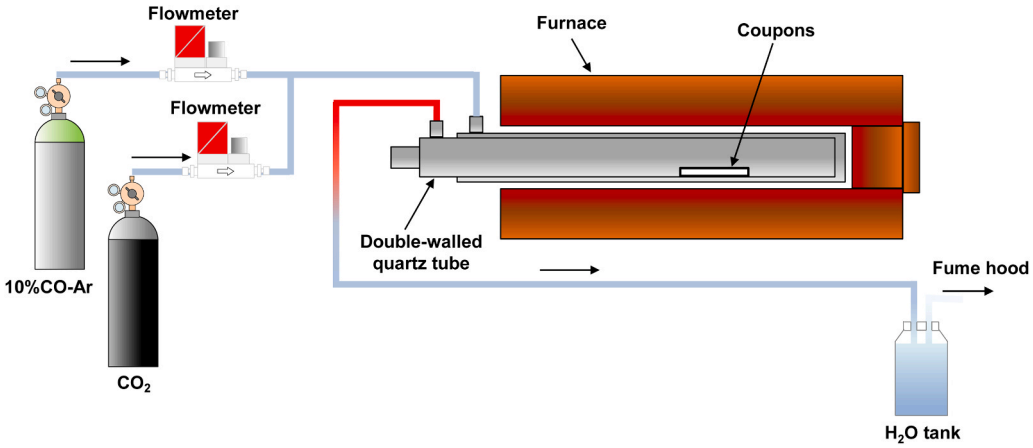

Fig. 1. Schematic of the mixed gas reaction rig.

and 5000×, respectively). Note that these calculations are based on thermodynamic conditions only, and do not consider the kinetics of gas phase reactions, which is important and will be discussed later. The flow rate of both gases can be determined by setting the total flow rate to be approximately 30 ml/min, Table 2. For laboratory safety and flammability limits, a 10 %CO-Ar mixture was used instead of pure CO.

$$\frac{p_{CO_2}}{p_{CO}} = p_{O_2}^{1/2} \exp\left(\frac{-\Delta G_{f.CO_2}}{R \bullet T}\right) \quad (2)$$

The testing procedure involved placing polished and ultrasonically cleaned samples in a ceramic boat inside the glass tube, with a thermocouple positioned approximately 10 mm from the samples. The tube was purged with high-purity argon gas for one hour before heating. Once the temperature stabilized at 480 °C, a 10 % CO-Ar mixture was introduced for 20 minutes via computer-controlled flowmeters, followed by CO_2 for another 20 minutes, also via flowmeter. The argon flow was then stopped, initiating the experiment. To terminate the experiment, argon was reintroduced for 20 minutes, the CO_2 flow was stopped, and the CO flow was ceased after an additional 20 minutes. Argon continued to flow until the temperature dropped to 200 °C, and the samples were removed the next day.

2.3. Microstructural characterization

Post-exposure characterization was performed using various complementary microscopy techniques. The surfaces of oxidized samples were initially inspected using scanning electron microscopy (SEM) on a FEI FEG-Nova NanoSEM located at Reactor Materials Testing Laboratory (RMTL), Queen's University, Kingston, ON, Canada. The micrographs were captured at 10 kV and with a working distance of 5 mm. Two site-specific FIB trenches from each sample were prepared with a LEO-Zeiss 1540 FIB-SEM located at the Nanofabrication Facility, University of Western Ontario, London, ON, Canada with the objective of assessing whether internal/intergranular oxidation occurred in multiple areas prior to TEM analysis. After confirmation of internal and intergranular oxidation in FIB trenches [50], one oxidized grain boundary from each sample was extracted for TEM examination. A conventional FIB lift-out procedure was used for TEM sample preparation on a Thermo Fisher Helios 5 UC FIB-SEM from the Canadian Centre for Electron Microscopy (CCEM), Hamilton, ON, Canada. All foils were extracted from high-angle grain boundaries, as more intense PIO is expected at these boundaries. TEM analysis was conducted using a FEI Osiris FEG-TEM with an accelerating voltage of 200 kV, located at RMTL. Electron energy loss spectroscopy (EELS) analysis was performed using a Thermo Fisher Scientific Spectra Ultra S/TEM operated at 200 kV, equipped with a Gatan Imaging Filter (GIF) Continuum K3® HR from CCEM. All TEM analyses were conducted with the grain boundaries aligned generally parallel to the beam. The convergence semi-angle was 28 mrad, and the collection semi-angle was 47.8 mrad, with an energy dispersion of 0.05 eV/channel, an exposure time of ~1.5 ms/pixel, and a step size of 1 nm was used for Zero Loss Peaks (ZLP). For the core loss spectra, an energy dispersion of 0.09 eV/channel, exposure of 0.4 s/pixel, and step size of 0.13–2.5 nm were used. The spectrum image (SI) was processed using Gatan Digital Micrograph, version 3.5. The dimensionality of the data was reduced by performing multivariate statistical analysis (MSA) on the spectrum image.

Table 2
Test conditions used for experiments in this study.

Test condition	Temp. [°C]	CO_2/CO ratio	Below Ni/NiO equilibrium	Flow rate 10 % CO-Ar [ml/min]	Flow rate CO_2 [ml/min]	Time [h]
500× 5000×	480	110.13 34.83	500 5000	2.50 7.00	28.08 24.87	192

3. Results

3.1. Baseline material characterization

The resulting microstructure after aging consisted of equiaxed grains with an average grain size of 40 μm, Fig. 2a. Selected area diffraction pattern (SADP) of [110] pole performed on the aged specimen confirmed the presence of the γ' superlattice reflection, Fig. 2b. The carbide distribution plays an important role in PWSCC resistance, and the HTH heat treatment is known to result in blocky Nb/Ti-rich MC-type intragranular carbides, along with $M_{23}C_6$ globular, discrete, and cellular intergranular carbides [11,12,54]. The cellular carbides consist of

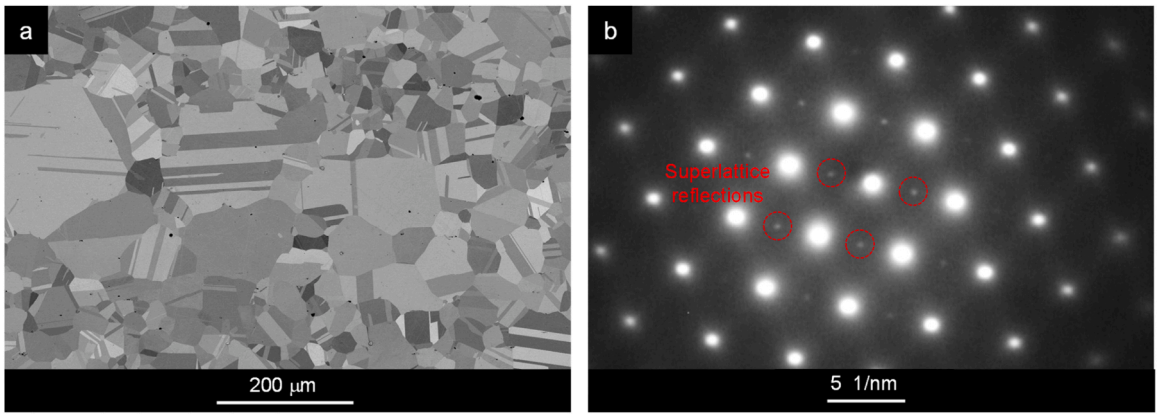

Fig. 2. (a) Secondary electron (SE) SEM micrograph of an aged Alloy X-750 sample, and (b) [110] SADP pattern from an aged Alloy X-750 sample showing the γ' superlattice reflections.

alternating layers of carbide and γ'-free solid solution, and its precipitation is reported to be promoted by cold work or water quenching after annealing [54,55]. The three types of intergranular carbides observed after HTH treatment are shown in Fig. 3: (a) discrete, (b) cellular, and (c) globular carbides.

3.2. SEM characterization of surface film

Typical secondary electron (SE) and backscattered electron (BSE) micrographs showing the surface morphologies of the samples after exposure to CO-CO_2 environments for 192 h at 480 °C are shown in and Fig. 4 and Fig. 5 for 500× and 5000× testing conditions, respectively. The BSE images indicate that the grain boundaries were likely oxidized due to their darker appearance (low Z element present such as oxygen). SEM examination of the oxidized samples tested at 500× reveals the presence of an external oxide, confirmed with chemical characterization,. In addition to the oxide film, the surfaces present globular features that resemble metallic Ni nodules [33,53]. However, the presence of whiskers on the surface suggests that these are stable oxides. Notably, even though the environment was calculated to be thermodynamically below the Ni/NiO equilibrium, no metallic Ni nodules were visible on the surface. The possible reasons for this discrepancy will be discussed later. At 5000×, *i.e.* more reducing conditions, the surface exhibits nodular features, which appear bright in BSE imaging, consistent with Ni nodules observed in previous studies [33,53], Fig. 5; enrichment of Ni will be confirmed in TEM analysis of Section 3.3. Hence, in the 5000× environment, with lower oxygen partial pressure, the system likely can attain the thermodynamically expected reducing conditions, in the Ni-metal stable regime. In Fig. 5c, an undulated grain boundary associated with DIGM is visible, DIGM is the lateral motion of the grain boundary resultant from the outward diffusion of more reactive elements [29,56]. Similar DIGM has been frequently observed in Alloy 600 tested in 480 °C H_2-steam, and it is considered a precursor to PIO and ultimately PWSCC [41].

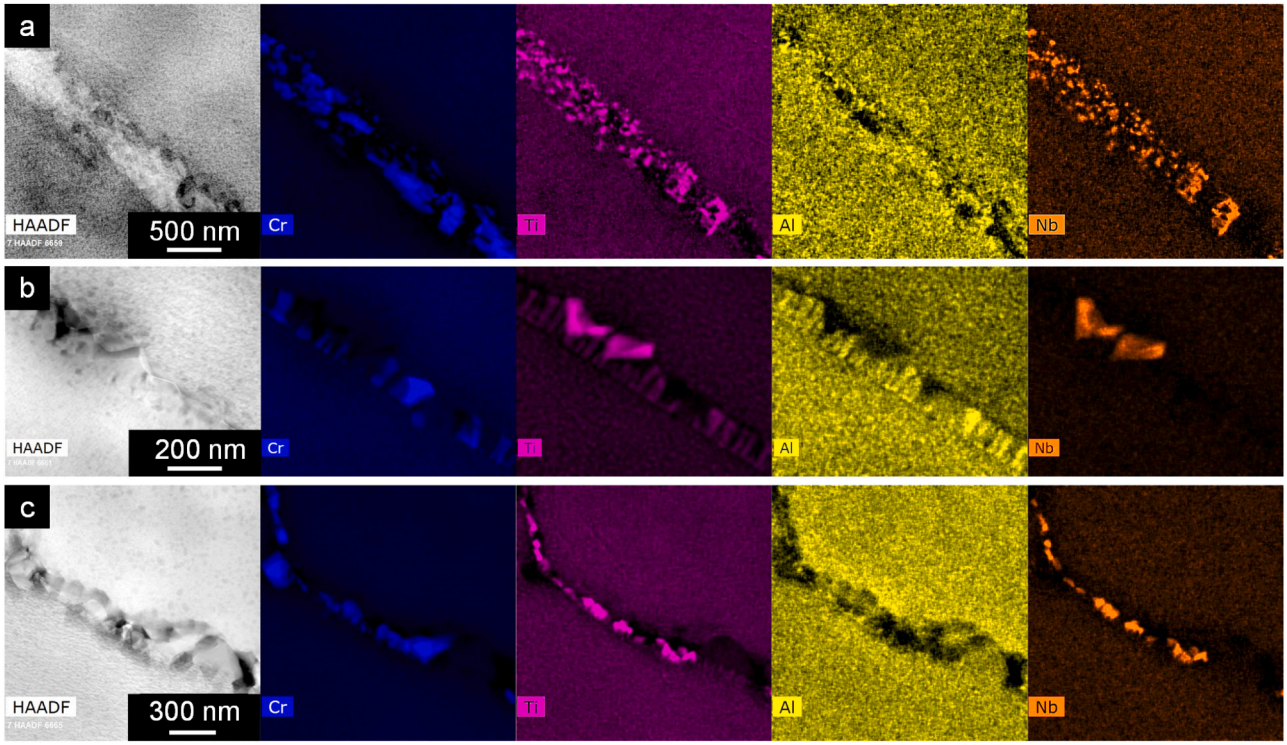

Fig. 3. Different intergranular carbide morphologies observed after HTH treatment: (a) discrete, (b) cellular, and (c) globular carbides.

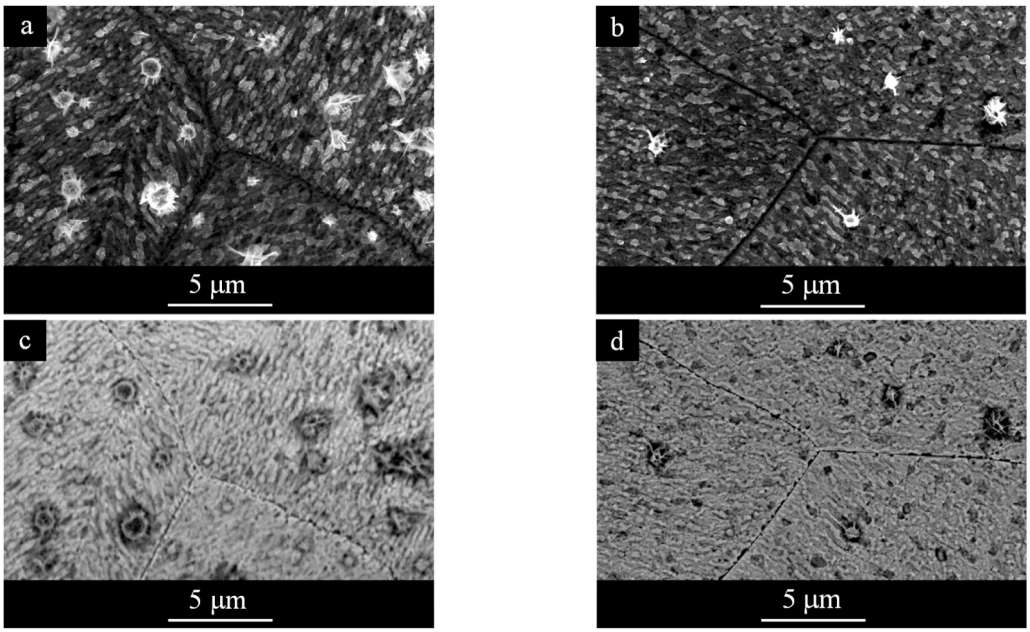

Fig. 4. (a) Secondary electron (SE) and (c) backscatter electron (BSE) SEM micrographs from an aged X-750 sample. (b) SE and (d) BSE micrographs from an annealed X-750 sample. These samples were exposed to the 500× testing condition for 192 h at 480 °C.

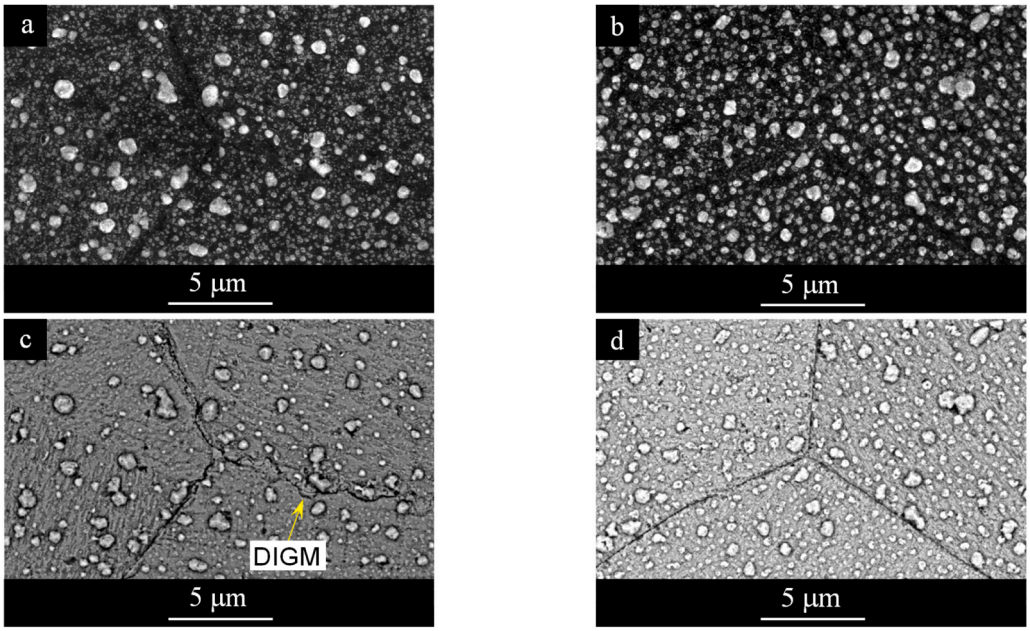

Fig. 5. (a) SE and (c) BSE micrographs from an aged X-750 sample. (b) SE and (d) BSE micrographs from an annealed X-750 sample. These samples were exposed to the 5000× testing condition for 192 h at 480 °C.

3.3. Analytical transmission electron microscopy (TEM) analysis

TEM samples were prepared to further investigate the internal and intergranular oxidation for each sample and test condition: annealed and aged at 500× and 5000×. Fig. 6 shows high-angle annular dark-field (HAADF) images of the region of interest for the four TEM foils, one from each sample. Note that prior FIB-trenching across several boundaries confirmed similar intergranular oxidation behaviour, shown in previous work [50]. A dark phase is observed under the surface and along grain boundaries, suggesting an oxide has formed based on Z contrast. Also, there are surface oxides and/or Ni nodules formed on the surface. The samples tested at 500× developed an acicular oxide on the surface of both annealed and aged samples; this oxide morphology is described as whiskers or blades [57,58]. Additionally, the TEM micrographs indicate the occurrence of internal oxidation due to the porous appearance of samples close to the surface. The scanning TEM (STEM)-EDX elemental maps of the annealed Alloy X-750 tested at 500× confirm that internal oxidation of Cr and Ti occurred, which is commonly observed in high-temperature experiments (800–1000 °C) [59,60], with the formation of whiskers and external oxides of Ni and Fe on the surface, Fig. 7. Although Ni was not oxidized below the surface oxide, a layer of spinel oxide is present, and no metallic Ni nodules were identified on the surface, unlike commonly reported in Alloy 600 exposed to H_2-steam. The absence of Ni nodules on the surface indicates that although the

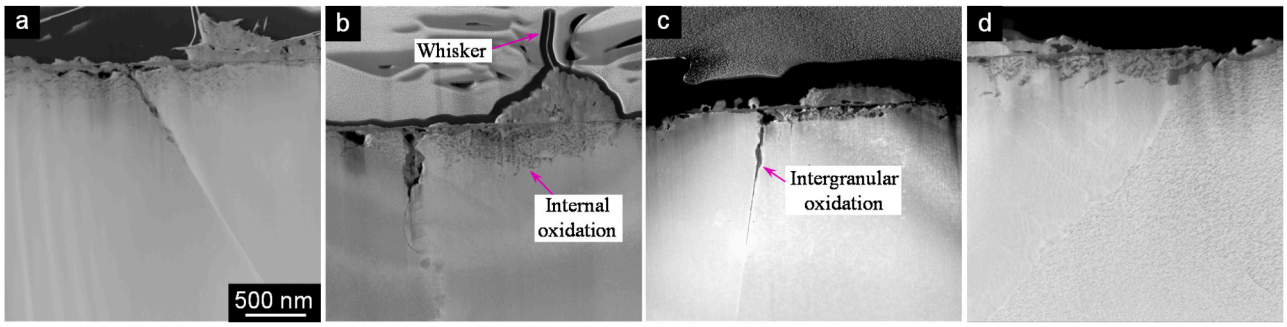

Fig. 6. High-angle annular dark-field (HAADF) images of TEM samples containing the regions of interest. TEM samples from the following exposure conditions are shown: (a) annealed Alloy X-750 at 500×; (b) aged Alloy X-750 at 500× with whisker oxide and internal oxidation; (c) annealed Alloy X-750 at 5000× with clear intergranular oxidation; and (d) aged Alloy X-750 at 5000×. The scale bar in (a) is applicable to all figures.

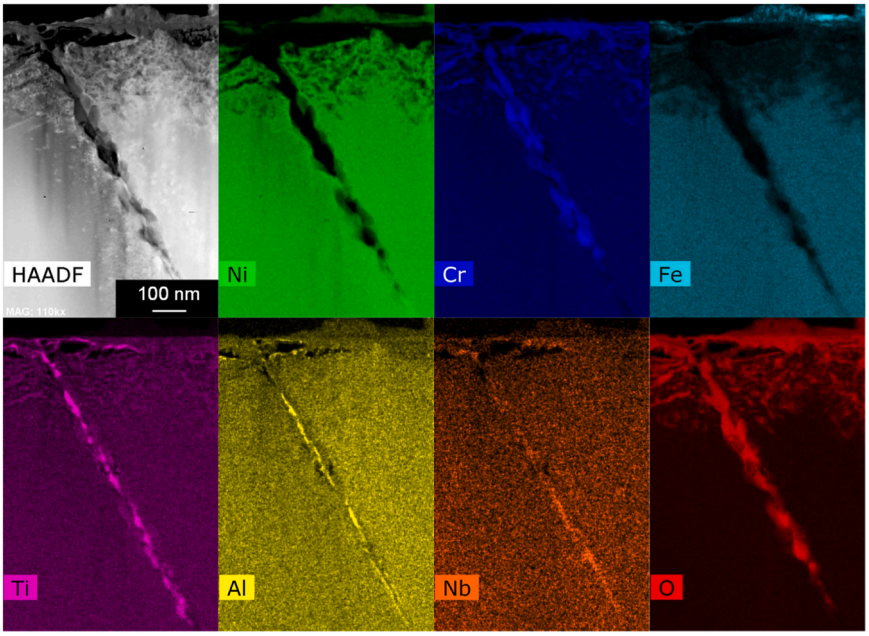

Fig. 7. STEM-HAADF image and EDX elemental maps showing internal oxidation of solute reactive elements within the grains and intergranular oxidation along a grain boundary from an annealed Alloy X-750 sample tested at 500× for 192 h at 480 °C.

environment was thermodynamically calculated to be reducing for Ni, the gas mixture was able to oxidize Ni during the experiment, for reasons that will be discussed later. Below the thick Fe/Ni oxide, Cr is internally oxidized, noting the discrete particles, along with the formation of a thin Cr oxide at the surface of the material. No intergranular carbides were visible, which is consistent with the literature, which states that annealing at 1093 °C dissolves the majority $M_{23}C_6$ carbides in Alloy X-750, [61]. Due to the absence of intergranular carbides, the intergranular oxidation is unimpeded, and penetrates approximately 1 μm deep. The intergranular oxidation front is led by the oxidation of Ti, along with Al and Nb. Intergranular oxidation of Cr takes place closer to the surface, and appears to surround the Al, Ti, and Nb rich oxides, while Fe is oxidized at the surface. The PIO observed is similar to that observed in Alloy 600 in the solution annealed condition exposed to 480 °C H_2-steam [29], although the oxidation of Al and Ti is less prominent in Alloy 600 and coincides with Cr oxidation. EELS elemental maps at the tip of the intergranular oxidation front show elemental distribution in the oxide, Fig. 8a. At this higher resolution, Ti and Al oxidation is clearly visible at the intergranular oxidation front, while Cr is depleted, shown by the line scan indicated by the red arrow, Fig. 8b. In contrast to the surface, Ni remains metallic and is enriched ahead of the intergranular oxidation front, whereas Cr is depleted, confirmed by line scan in the yellow arrow and shown in Fig. 8c; this is consistent with observations in Alloy 600, [30,41]. The oxygen partial pressure at the intergranular oxidation front would be lower compared with the surface which explains why Ni remains metallic ahead of the intergranular oxide.

On the surface of the aged Alloy X-750 sample tested at 500×, in Fig. 9, a prominent nodule-like feature is visible. The EDX elemental maps reveal that this feature is composed of Ni and Fe oxide, with Fe concentrated on its outer surface. Similarly to the annealed sample, Fe/Ni whisker oxides are formed on the surface of the aged sample. The intergranular oxidation of the aged Alloy X-750 sample tested at 500× has two distinct morphologies. Closer to the surface, a thicker intergranular oxide is formed. Below that, a fine intergranular oxide is formed with a tortuous path contouring the intergranular cellular carbides, Fig. 10a. At higher magnification, EELS elemental maps reveal further details about the microstructure and intergranular oxidation, Fig. 10b. Within the matrix, γ' precipitates are visible, revealed in Ti and Al maps with a spherical shape and an approximate diameter of 10 nm. Neighbouring the fine intergranular oxidation, the solid solution that alternates with the cellular carbides is depleted in Ti and Al, which likely diffused to the grain boundary and formed the intergranular oxide, as shown by the line scan in Fig. 10c. The intergranular oxide is also depleted in Fe and Cr which diffused towards the surface, while Ni

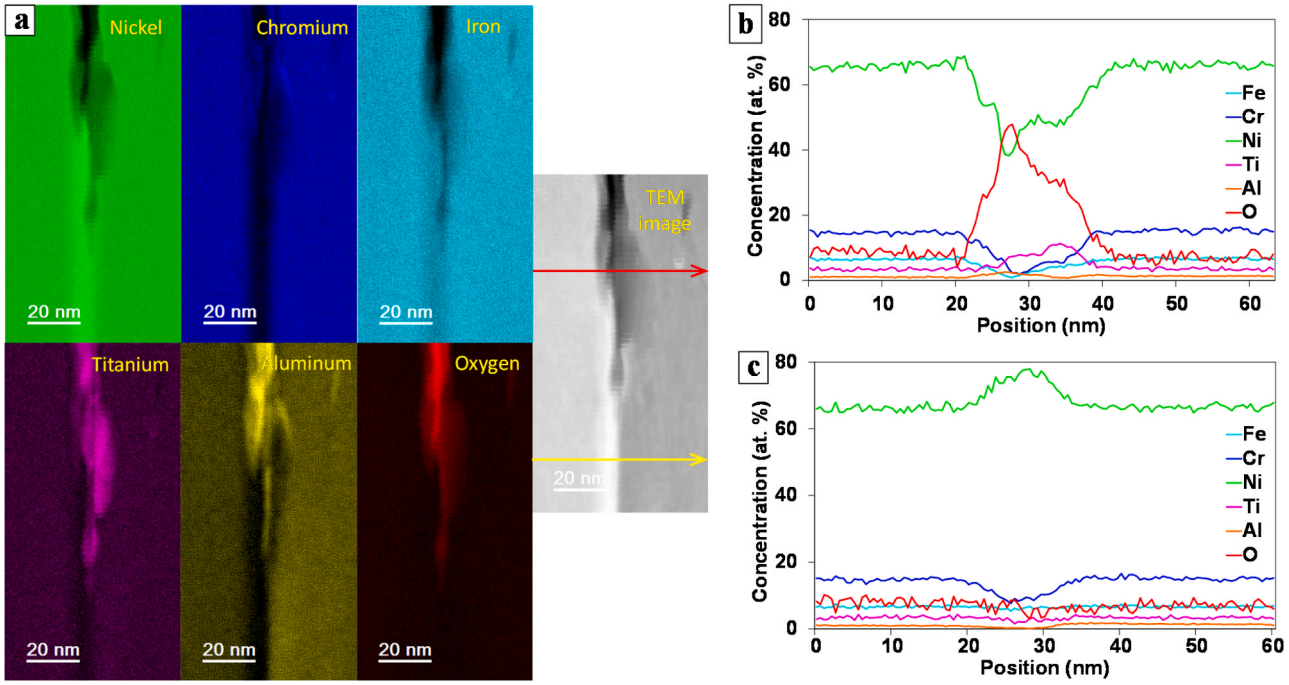

Fig. 8. (a) EELS elemental maps of the tip of intergranular oxidation from an annealed Alloy X-750 sample tested at 500× for 192 h at 480 °C, (b) quantitative line scan across the red arrow in (a) at the intergranular oxidation, and (c) quantitative line scan across the yellow arrow in (a) ahead of the intergranular oxidation.

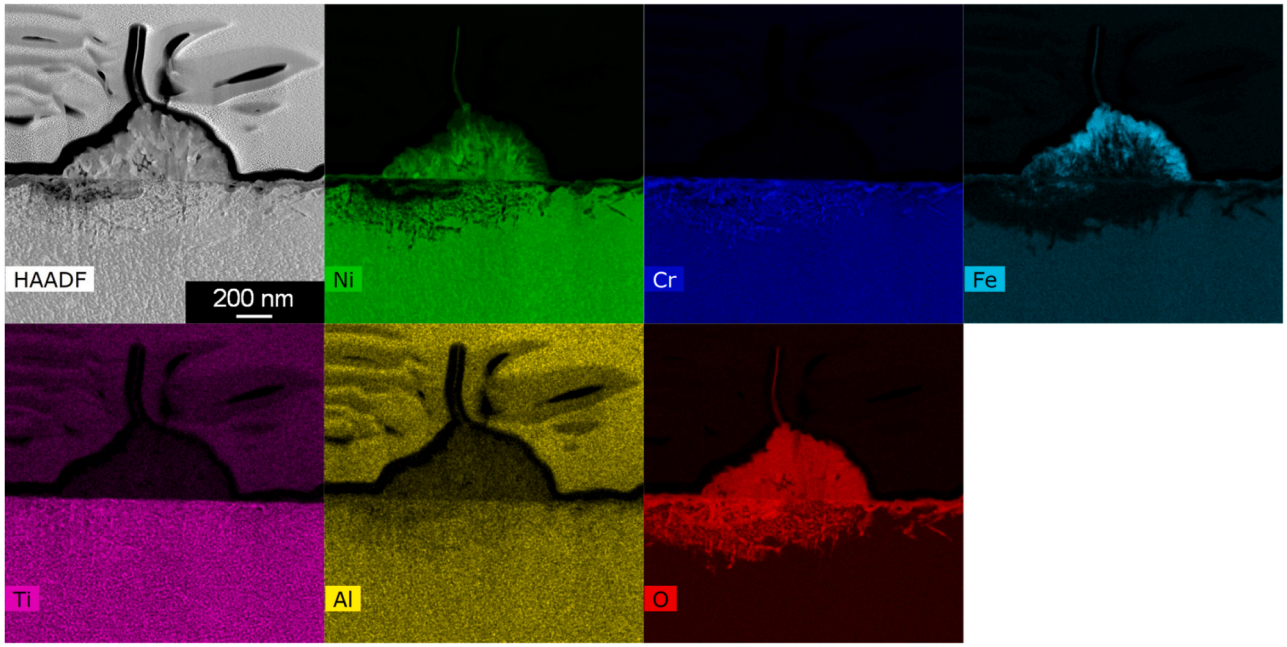

Fig. 9. EDX elemental maps showing internal oxidation beneath the surface and a Ni/Fe superficial globular oxide formed on an aged Alloy X-750 sample tested at 500× for 192 h at 480 °C.

diffused either to the surface or ahead of the intergranular oxidation. The tip of the intergranular oxidation stops at a Ti/Cr-rich carbide, which also confirms the role of Ti and Al in leading the oxidation, Fig. 11.

Similar to the sample tested in the 500× condition, the STEM-EDX maps for the annealed Alloy X-750 sample tested at 5000× also shows a straight intergranular oxidation, initiated by Ti and Al, which appear in the core of the PIO and ahead of the Cr oxide with a depth of 1.1 μm, Fig. 12. The intergranular oxidation appears slightly curved, which may indicate the occurrence of DIGM, due to the outward diffusion of Fe and Cr, frequently reported in Alloy 600 [41,42]. Similar to the annealed X-750 sample tested at 500×, no intergranular carbides were present, confirming that during the exposure at this temperature there is no carbide formation. A large difference in intergranular oxidation penetration is observed when comparing the annealed Alloy X-750 sample with the aged sample tested in the 5000× condition, Fig. 13. Instead of the deep penetration observed on the annealed sample, the intergranular oxidation is shallower than the internal oxidation. Although the carbides were not as clear in Fig. 13 compared to Fig. 10, there were Ti-Nb enriched clusters at the grain boundary, indicating the presence of

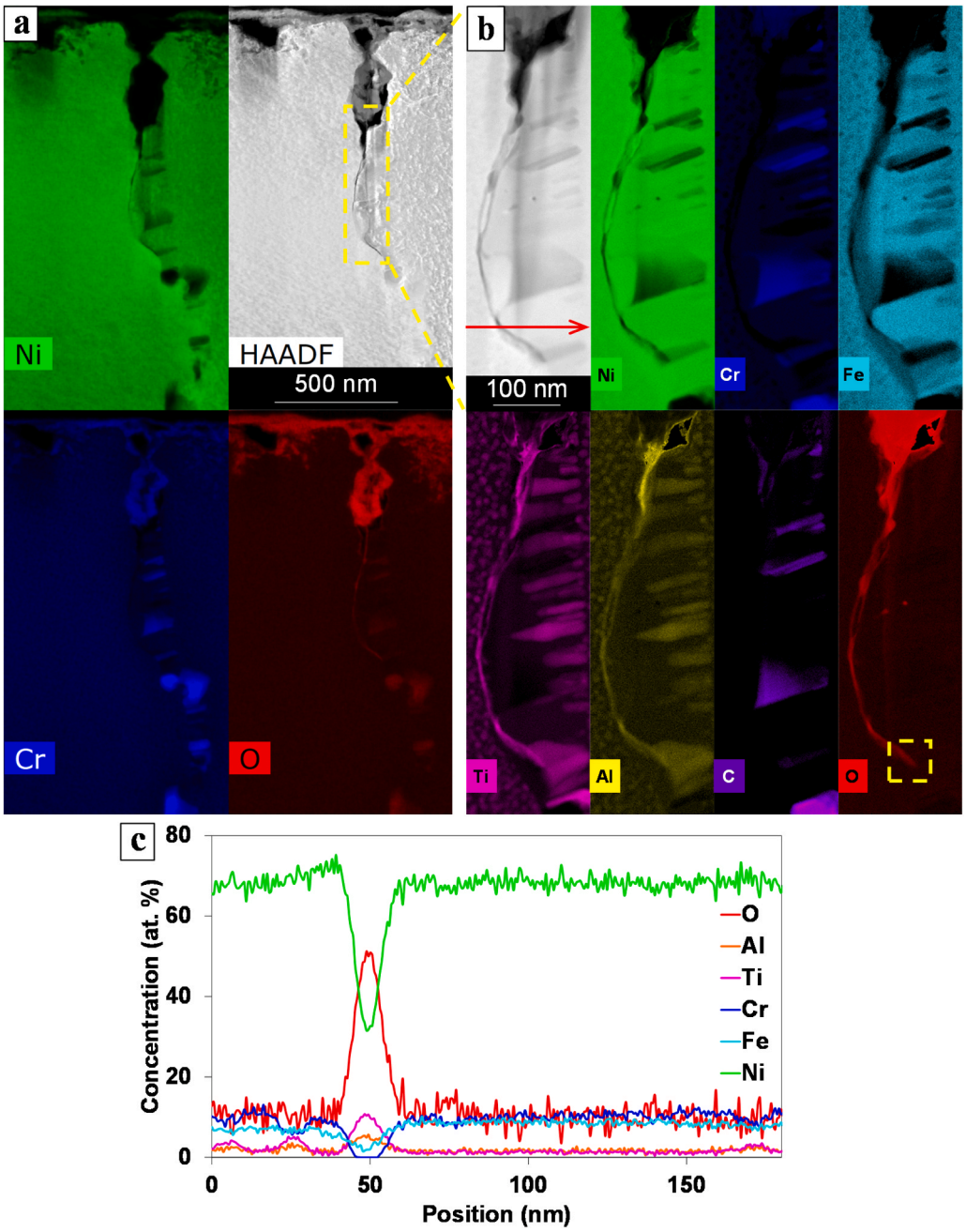

Fig. 10. (a) EDX elemental maps showing intergranular oxidation along a grain boundary on an aged Alloy X-750 sample tested in the 500× condition for 192 h at 480 °C. (b) EELS elemental maps showing intergranular oxidation initiated by Ti and Al. The carbon map also clearly shows the presence of cellular carbides. The oxygen map indicates the area around the tip of the intergranular oxidation from which the EELS elemental maps shown in Fig. 11 were obtained. (c) quantitative EELS line scan across the red arrow in (a) showing depletion of Ni, Fe and Cr, alongside enrichment in Ti and Al (approximately 50 nm wide).

cellular carbides, which can explain the limited intergranular oxide penetration of ≅ 300 nm. Similar to Fig. 8, a prominent Ni enrichment is visible in front of the intergranular oxide, Fig. 13. On the surface, the STEM-EDX maps and diffraction pattern (DP) confirm the presence of a Ni nodule covered by Ni oxide, Fig. 14b-c. Additionally, small spinel Ni-Fe oxides with a nodular shape were present on the surface, with a DP consistent with $NiFe_2O_4$ (trevorite). These nodular oxides were particularly noticeable on the annealed sample tested at 5000× as shown in Fig. 5b. At the tip of the tortuous intergranular oxidation, again, a mixture of Ti and Al oxide(s) is evident, confirming the prominent role of these elements in leading intergranular oxidation, Fig. 15.

4. Discussion

4.1. Internal and intergranular oxidation susceptibility of Alloy X-750 in a 480 °C CO-CO_2 environment

The results of this study show the nanoscale chemistry and morphology of PIO formed Alloy X-750 exposed to CO-CO_2 dry gas mixtures at 480 °C. This finding suggests that embrittlement of Alloy X-750 spacers in CANDU nuclear plants can be induced if the AGS were to transition towards reducing conditions (e.g., off-chemistry loss of oxygen or ingress of deuterium) [21,23]. The PIO and Ni nodule formation on the surface of Alloy X-750 in 480 °C CO-CO_2 are similar to the observations for Alloy 600 tested in 480 °C H_2-steam [29,44]. In fact, these

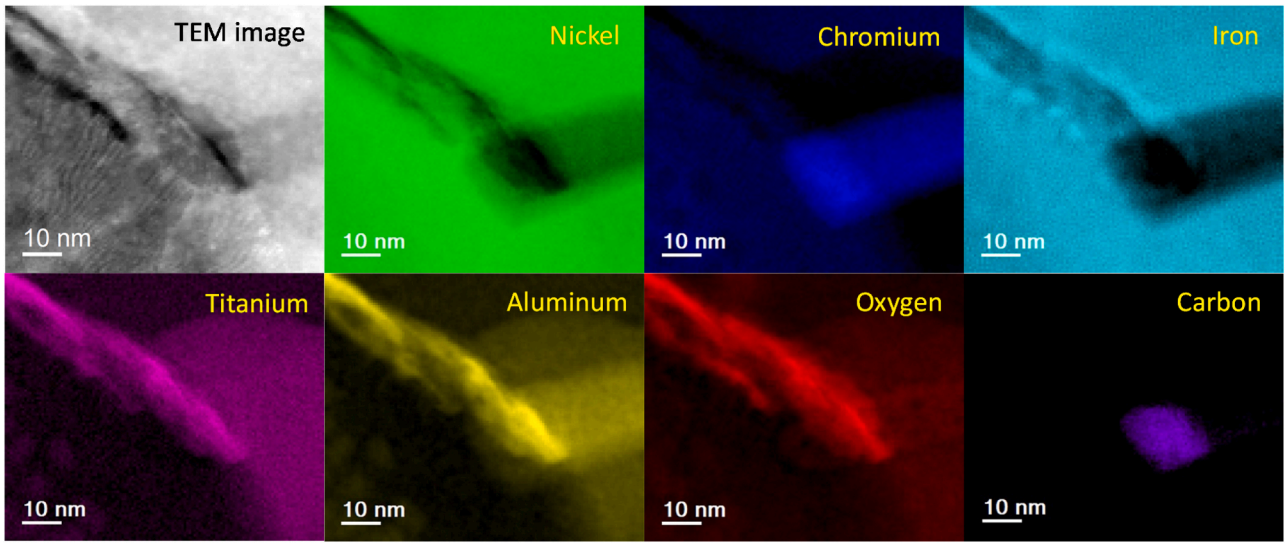

Fig. 11. EELS elemental maps of the tip of the intergranular oxidation formed in an aged Alloy X-750 sample tested in the 500× condition for 192 h at 480 °C, confirming Ti and Al oxide formation along with a general lack of Cr oxidation. The intergranular oxide arrests at the cellular carbide.

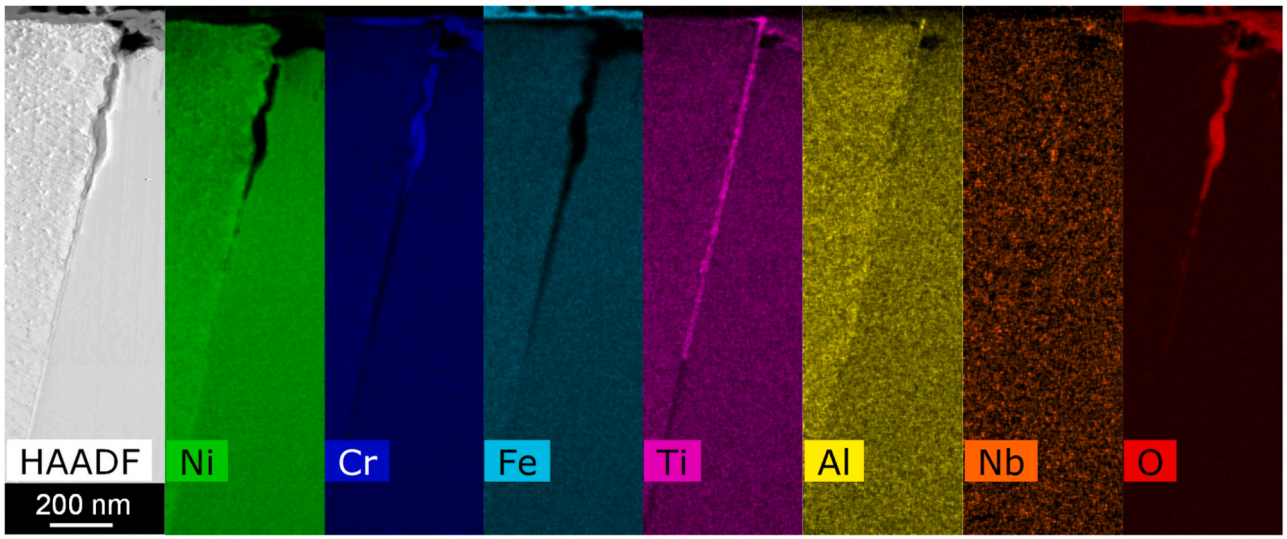

Fig. 12. STEM-EDX elemental maps showing intergranular oxidation along a grain boundary formed in an annealed Alloy X-750 sample tested at 5000× for 192 h at 480 °C.

features are believed to be the precursors to intergranular PWSCC, and therefore similar observations for Alloy X-750 in CO-CO_2 suggests that intergranular cracking may also be possible. Although the reaction kinetics of H_2-steam and CO-CO_2 are not equivalent, and Alloy X-750 is a precipitation hardened alloy, from a pure thermodynamic point of view, hydrogenated steam and CO-CO_2 appear to behave in a similar manner.

Fig. 9 shows that the globular formation on the surface of Alloy X-750 samples tested in the 500× condition is a Ni/Fe oxide rather than a metallic Ni nodule. This EDX map indicates that although the environment was thermodynamically calculated to be reducing for Ni, the element was in fact oxidized. This superficial Ni oxidation may have a few different explanations. Firstly, the oxygen partial pressure to form Ni-containing spinel oxides is lower than that of NiO. At least two spinel oxides may form, $NiFe_2O_4$ (trevorite) and $NiCr_2O_4$ (nichromite), which can precipitate at lower oxygen partial pressure in comparison to NiO [37,38]; this is supported by the DP of $NiFe_2O_4$ spinel oxide shown in Fig. 14a. Secondly, although high-purity gases were used in the experiments, small concentrations of oxygen are always present. A few additional parts per billion of oxygen in the gas mixture will increase the oxygen partial pressure, possibly shifting to an oxidizing environment for Ni rather than reducing, and therefore the oxygen partial pressure in the environment is not completely buffered by the CO/CO_2 mixture. The gas supplier data sheet specifies a maximum oxygen concentration of 2 parts per million (ppm) for Ar and CO_2, and 10 ppm for CO. Nevertheless, these concentrations are specified as maxima and their exact values are uncertain. However, this ppm-level of oxygen would have also been present in 480 °C H_2-steam experiments for Alloy 600, where Ni oxidation was not observed [44]. A third explanation for the formation of an external oxide in the 500× testing condition is reaction kinetic limitations. Experiments performed in H_2-steam (using pure H_2) are generally performed with an oxygen partial pressure between 20 and 40 times below the NiO dissociation partial pressure [53,62]. From a thermodynamic perspective, the oxidation of CO is more favorable than H_2, which is evident from the Ellingham diagram (Gibbs free energy more negative). However, kinetically, the oxidation of CO is very slow, with a much higher activation energy in comparison with the oxidation of H_2 [63]. For this reason, the experiments in CO-CO_2 mixtures have to be more reducing in comparison to H_2-steam environments to overcome

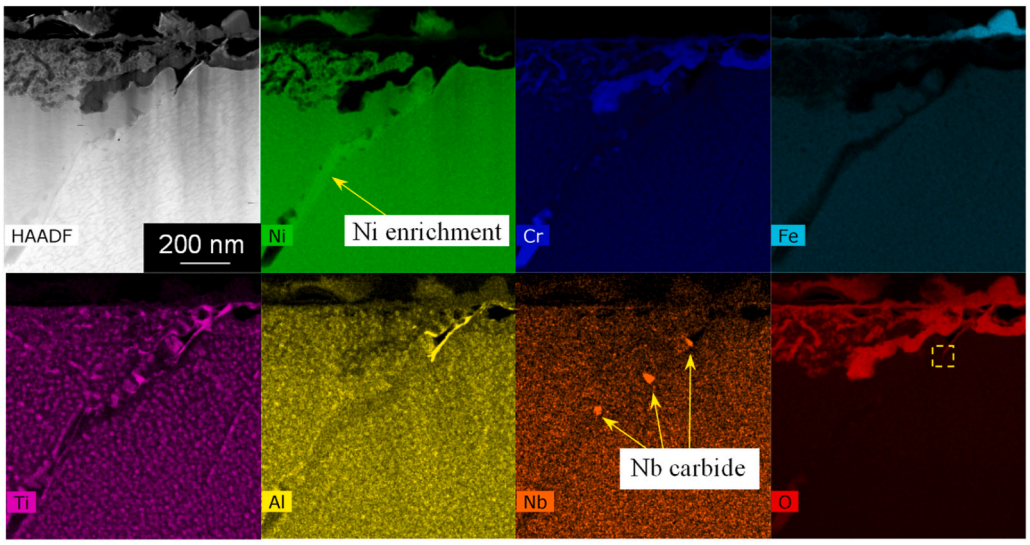

Fig. 13. STEM-EDX elemental maps showing intergranular oxidation along a grain boundary formed in an aged Alloy X-750 sample tested at 5000× for 192 h at 480 °C. The oxygen map indicates the area around the tip of the intergranular oxidation from which the EELS elemental maps shown in Fig. 15 were obtained.

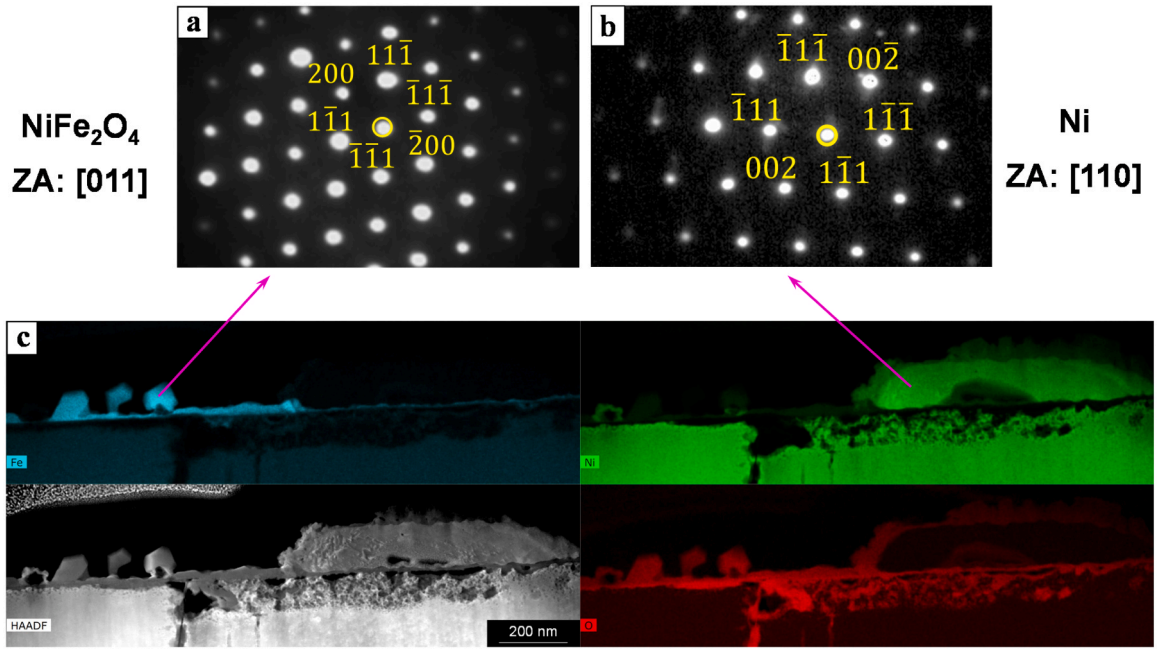

Fig. 14. Diffraction pattern for (a) the $NiFe_2O_4$ spinel oxide and (b) Ni nodule; (c) STEM-EDX elemental maps showing Ni nodule and spinel oxide formed on the surface of an annealed Alloy X-750 sample tested in the 5000× condition for 192 h at 480 °C.

limitations in the CO-CO_2 reaction kinetics. Another limitation could be the use of 10 %CO-Ar; even though the CO/CO_2 ratio is maintained, the partial pressure of CO and CO_2 available for reaction is much lower when compared with the use of a pure CO and CO_2 mixture, potentially altering the reaction kinetics. Therefore, although thermodynamic calculations suggest the environment should be reducing, reaction kinetics limitations probably result in more oxidizing conditions, especially when comparing the differences in reaction kinetics between the H_2-steam and CO-CO_2 reactions [63].

Despite the absence of Ni nodule formation on the surface, both internal and intergranular oxidation were still observed on annealed and aged Alloy X-750 samples tested in the 500× condition. This indicates that the testing environment (*i.e.*, at the sample surface) likely reached an oxygen partial pressure slightly higher than the Ni/NiO transition. However, below the external oxide layer, at the metal-oxide interface, the oxygen partial pressure was decreased, enabling the internal oxidation of reactive minor alloying elements, but not Ni, which remained metallic. Ni enrichment ahead of the intergranular oxidation front is observed in EDX/EELS maps and the line scan in Fig. 8, and this is generally thought to be due to outward diffusion of reactive elements during oxide formation [32,41]. It is however worth recalling that under specific conditions, pipe diffusion of metallic Ni to the outer surface can also occur as a stress relieving mechanism following the formation of internal oxide [64].

The surface of the Alloy X-750 samples tested at the 5000× condition showed clear Ni nodule formation; however, a nanometre-scale layer of Ni oxide is visible at the top of nodules on EDX maps, Fig. 14c. The presence of Ni nodules suggests that at this testing condition, the environment was reducing for Ni during the experiment, and the presence of Ni oxide suggests subsequent oxidation. Superficial (nanoscale) external

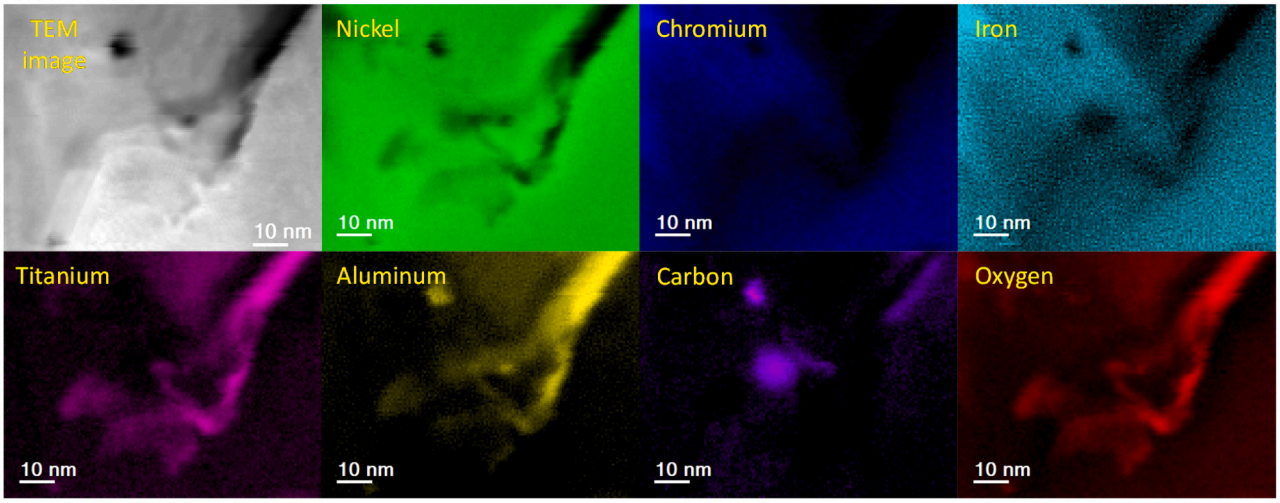

Fig. 15. EELS elemental maps of the tip of the intergranular oxidation formed in an aged Alloy X-750 sample tested in the 5000× condition for 192 h at 480 °C.

oxidation may occur while the system cools down at the end of the experiment, considering that the cool down was performed with high-purity argon gas until the internal temperature reached 200 °C and that the Ni/NiO oxygen equilibrium partial pressure decreases at lower temperatures. Hence, the environment was reducing at 480 °C but became oxidizing during cooling for a brief period, leading to a thin, unavoidable oxide film on Ni nodules due to limited diffusion and reaction kinetics, with high-purity argon containing up to 2 ppm of oxygen.

4.2. The role of intergranular carbides and Ti/Al in intergranular oxidation

It is well known from previous studies in Alloy 600 that intergranular carbides play a significant role in hindering intergranular oxidation in a 480 °C H_2-steam environment and in high temperature water [31,65]. Furthermore, the PWSCC susceptibility of Alloy 600 thermally treated (with intergranular carbides) has consistently been shown to decrease compared with Alloy 600 in the solution annealed condition [31,33]. Moreover, a previously common AH heat treatment (annealing at 982 °C, stress equalizing at 885 °C for 24 h, aging at 704 °C for 20 h) [66,67] does not promote intergranular carbide precipitation and resulted in X-750 being highly susceptible to PWSCC [12,68]. Since the Cr content of Alloy 600 and X-750 is identical, it was expected that the presence of intergranular carbides in Alloy X-750 would play a similar role in hindering intergranular oxidation. As shown in Fig. 10 and Fig. 13, intergranular carbides do not prevent intergranular oxidation but rather reduce the penetration depth. In the 500× testing condition, a thin but clear oxygen penetration occurs between the matrix and cellular carbides at a grain boundary. While intergranular oxide growth stops at a carbide, as shown in Fig. 11, it would likely continue with a longer exposure time (*i.e.*, after complete carbide consumption). Despite the presence of intergranular carbides, the depth of intergranular oxidation on the aged and annealed samples in the 500× testing condition are similar, at approximately 1 micrometre. Cr depletion (sensitization) is known to occur due to carbide precipitation with both globular and cellular carbides, but more intense for the latter [55]. Nevertheless, sensitization was not a focus in this study as a contributor to PWSCC in X-750 because the AH treatment is highly susceptible to PWSCC despite the absence of intergranular carbides and, consequently, sensitization. Intergranular oxidation observations generally agree with reported behaviour of Alloy 600 in 480 °C H_2-steam in previous studies, with Ti and Al leading PIO and the beneficial effect of intergranular carbides on suppressing intergranular oxide penetration [31,33]. The similar depth of intergranular oxidation on annealed and aged samples tested at the 500× testing condition may be due to the fact that intergranular carbide precipitation is intermittent, meaning the regions absent of carbides, as is the case shown in Fig. 10, behaves similar to the annealed sample where intergranular oxidation is unobstructed, emphasizing the importance of intergranular carbides on intergranular oxidation kinetics.

Al and Ti are added to Alloy X-750 to form γ' Ni_3(Ti, Al) precipitates, which provide high strength and creep resistance. The observation of Ti and Al at the tip of the intergranular oxidation had been described previously in Alloy 600 (alongside Cr) [30,41], where Al and Ti are present as trace elements, generally at a composition less than 0.3 wt%. Alloy X-750, on the other hand, has a significant concentration of these reactive elements, 2.45 wt% and 0.68 wt% for Ti and Al, respectively, in this study. The higher Al and Ti content in X-750 enable testing to strongly confirm the role of these elements in initiating intergranular oxidation, as shown in Fig. 8 and Fig. 10, while Cr is oxidized closer to the surface. However, it is uncertain if Ti and Al are found at the tip of the intergranular oxidation due to the third-element effect or due to a decrease in oxygen partial pressure with oxide growth. Since Cr oxidizes closer to the surface, where the oxygen partial pressure is higher, the oxygen partial pressure decreases along the grain boundary, possibly allowing only for the oxidation of Ti and Al [69], in agreement with the Ellingham Diagram [70]. The third element effect [71] occurs when an alloy with two or more reactive elements are present, such as Cr and Al. In such cases, the outward diffusion of Cr reduces the inward flux of oxygen, enabling the formation of an Al oxide layer below the Cr oxide.

Although Ti and Al are mostly combined with Ni, forming γ' precipitates, they are also present in cellular carbides as both (Ti-Nb) carbides and in solid solution with Ni, Fe and Al. Despite intergranular carbide precipitation on aged samples, intergranular oxidation still occurs. As shown in Fig. 10b, the solid solution within the cellular carbides is depleted in Al and Ti close to the grain boundary, which appear to have diffused to the grain boundary and oxidized. Meanwhile, the EELS maps do not indicate a reduction of γ' precipitates close to the grain boundary, indicating that dissolving/disordering the γ' precipitates is less favourable than diffusing from the solid solution. Notably, this may change in a radiation field, where disordering and dissolution of γ'precipitates [24,25] may facilitate a higher flux of Al and Ti to grain boundaries; this will be explored in future work on irradiated Alloy X-750 materials in CO-CO_2 environments.

It is generally accepted that only Al, Cr and Si are able to form a protective oxide scale in Fe, Co or Ni alloys for high-temperature applications (above 500 °C) exposed to air [71–73]. Although Al is

reported to be beneficial in air by forming an Al_2O_3 layer [71,72], in primary water conditions studies suggest the opposite. Model Ni-based alloys (Ni-4 and 7 at% Al) tested in hydrogenated steam [74,75] and hydrogenated water [40] exhibited intergranular oxidation driven by Al oxidation. Moreover, experiments performed with Alloy 600 in hydrogenated steam also suggest that Al is detrimental by leading PIO along with Ti [30,41]. For Ti, it is suggested that the element has a detrimental effect in alloys oxidized in air at high temperatures [69,76–78], including by promoting intergranular oxidation [79,80]. It appears the same is true in reducing conditions for Ni alloys at 480 °C, supported by the results in hydrogenated steam [30,41] and the results presented in this work. Since the Alloy 600 samples used in studies with hydrogenated steam [30,41] have both Al and Ti, it is important to know if both are detrimental or if one oxide formed because another element oxidized first. However, as model Ni-alloy testing does not add Ti, the intergranular oxidation reported in the experiments performed by Ghaffari et al. [74,75] and Bruemmer et al. [40] was driven solely by Al, with no contribution of Ti.

4.3. The contribution of PIO to spacers' embrittlement

In accordance with prior research, when the oxygen partial pressure is decreased, a reducing CO-CO_2 environment can induce PIO of Alloy X-750 spacers [50]. The PIO could result in embrittlement of near-surface grain boundaries, potentially contributing to crack initiation. This contribution of PIO to embrittlement may be combined with the known irradiation embrittlement effects [24,26,27]. Since the spacer cross-section is small, 0.76 mm by 0.76 mm, PIO of just a few micrometres could be significant, as it would affect the entire external surface of the component. However, it is critical to emphasize that although a transient where oxygen is totally absent has not been reported in CANDU reactors with the current configuration of CO_2 plus 0.5–5 vol% O_2, it is relevant to mention that initially the AGS was filled with N_2 up until the 1980s when it shifted to (pure) CO_2 and finally to CO_2-O_2 at the beginning of 1990s [19]. Still, the current research should be considered proactive, only evaluating an extreme off-chemistry scenario for the AGS which, to the knowledge of the authors, has not occurred.

There is a constant ingress of deuterium (D_2) and moisture from the end fittings into the AGS. For this reason, the dew point is constantly monitored to detect moisture, and the system is purged periodically to remove these contaminants. As mentioned, in this project it was considered a hypothetical scenario where oxygen is absent. Hence, the ingress of deuterium would result in CO_2 being reduced to CO and the AGS would result in a mixture of CO, CO_2, D_2, and moisture. Although moisture would contribute to spacer oxidation, D_2 is a significantly more efficient reducing agent than CO, as discussed in terms of reaction kinetics in Section 4.1 [63]. This study shows that the reducing condition for internal oxidation must be extreme, at an oxygen partial pressure 5000× below the NiO dissociation pressure, and certainly not relevant to the AGS. As mentioned, the AGS is normally an oxidizing environment due to the addition of 0.5–5 vol% O_2. Alloy X-750 exhibits the highest PWSCC crack growth rate close to the Ni/NiO equilibrium electrode potential, meaning that highly oxidizing or reducing environments for Ni will decrease PIO contribution to embrittlement. It is also important to note that experiments at the 500× condition resulted in PIO despite the formation of external oxide, indicating that the exact window where PIO occurs in a CO-CO_2 mixture is still unclear (*i.e.*, conditions in the NiO stable regime at the surface can still result in internal and intergranular oxidation in the metal if the oxygen partial pressure at the metal-oxide interface is sufficiently decreased). Hence, the formation of an external oxide layer did not prevent the oxidation of Al and Ti along grain boundaries with subsequent PIO, suggesting that a higher Cr content is necessary to more rapidly form an oxide protective layer to prevent oxygen penetration along grain boundaries. Regardless, even the 500× testing condition is extremely reducing compared to the AGS, so even with minor ingress of D_2 or brief loss of oxygen it seems unlikely that a thermodynamic condition near the Ni/NiO equilibrium oxygen partial pressure will be attained in the AGS.

5. Conclusions

1. Reducing 480 °C CO-CO_2 mixtures promote both internal and intergranular oxidation of Alloy X-750, and could contribute to spacer embrittlement for crack initiation, but only in a hypothetical scenario where O_2 is absent, and the environment becomes sufficiently reducing. Such a condition does not seem relevant to the AGS at the present time.
2. The depth of intergranular oxidation in Alloy X-750 tested in the 500× condition was comparable for aged and annealed samples. At 5000×, however, the depth of intergranular oxidation in the annealed X-750 samples was almost four times as deep compared to the aged sample.
3. The intergranular oxidation front is led by Ti and Al oxidation, suggesting a detrimental effect of these minor elements on PIO, while the presence of intergranular cellular carbides hinders intergranular oxidation.
4. The solid solution present adjacent to cellular carbides can better supply Al and Ti to the grain boundaries compared with γ' precipitates. However, in the presence of a radiation field this is likely to change due to radiation-induced disordering and dissolution of γ' precipitates.
5. Annealed samples presented a larger number of nodular features on the surface of the samples tested at 5000× in comparison to the aged samples, which were revealed to be a combination of Ni nodules and Ni-Fe spinel oxides.

CRediT authorship contribution statement

Suraj Y. Persaud: Writing – review & editing, Supervision, Project administration, Methodology, Investigation, Funding acquisition, Conceptualization. **Fabio Scenini**: Writing – review & editing, Methodology, Investigation, Conceptualization. **Liberato Volpe**: Writing – review & editing, Methodology. **Adriano Eidi Yaedu**: Writing – original draft, Investigation, Formal analysis. **Adil Shaik**: Investigation. **Kevin Daub**: Writing – review & editing, Resources, Methodology, Investigation, Conceptualization. **Fei Long**: Investigation.

Declaration of Competing Interest

The authors declare the following financial interests/personal relationships which may be considered as potential competing interests: Adriano Eidi Yaedu reports financial support was provided by University Network of Excellence in Nuclear Engineering. Adriano Eidi Yaedu reports financial support was provided by Natural Sciences and Engineering Research Council of Canada. Adriano Eidi Yaedu reports equipment, drugs, or supplies was provided by Haynes International Inc. If there are other authors, they declare that they have no known competing financial interests or personal relationships that could have appeared to influence the work reported in this paper.

Data availability

Data will be made available on request.

Acknowledgments

The authors would like to acknowledge the financial support of The University Network of Excellence in Nuclear Engineering (UNENE) and Natural Sciences and Engineering Research Council of Canada (NSERC). This work was also supported by the Henry Royce Institute for Advanced Materials, funded through EPSRC grants EP/R00661X/1 and EP/P025021/1. The authors are thankful to Haynes International for

providing the Alloy X-750 samples employed in this work. The authors acknowledge Travis Casagrande and Sabaa Rashid at the Canadian Centre of Electron Microscopy (CCEM) at McMaster University for FIB sample preparation and Natalie Hamada for the EELS analysis. The authors would like to thank Dr. Mark Daymond for providing SEM and TEM access at the Reactor Materials Testing Laboratory (RMTL) at Queen's University.

References

[1] T. Yonezawa, Nickel Alloys: Properties and Characteristics," in, in: R.J.M. Konings, R.E. Stoller (Eds.), Comprehensive Nuclear Materials, Elsevier, 2020, pp. 319–354.
[2] G.D. Smith, B.A. Baker, Nickel and its Alloys, in: M. Kutz (Ed.), in Mechanical Engineers' Handbook, Volume 1 - Materials and Engineering Mechanics, fourth ed, John Wiley & Sons, 2015.
[3] A.A. Stein, M.S. Gennaro, and J.L. Nelson, "Material specification for Alloy X-750 for use in LWR internal components (Revision 1)," 1990, *EPRI NP-7032, Palo Alto, CA*.
[4] A.A. Stein, I. Sprung, M.S. Gennaro, and J.L. Nelson, "Design and manufacturing guidelines for high-strength components in LWRs - Alloy X-750," 1991, *Palo Alto, CA*.
[5] R.A. Chaplin, et al., The Essential CANDU, UNENE, 2014.
[6] L. Marc, P. Nandu, S. Basma, 2012, , The technology of CANDU fuel channels.
[7] H. Coriou, L. Grall, Y.Le Gall, and S. Vettier, "Corrosion fissurante sous contrainte de l'Inconel dans l'eau à haute température," Saclay, 1960.
[8] J. Blanchet, H. Coriou, L. Grall, C. Mahieu, C. Otter, G. Turluer, Influence de la contrainte, des traitements thermiques et des couplages sur la fissuration intergranulaire des alliages 1nconel 600 et X 750, J. Nucl. Mater. vol. 55 (2) (1975) 187–206, https://doi.org/10.1016/0022-3115(75)90152-X.
[9] T.M. Anderson, 1979, , NS-TMA-2099 - Reactor Internals - Cracked Pins and Flexures in Guide Tubes.
[10] E.L. Jordan, "Control rod drive (CRD) guide tube support pin failures at Westinghouse PWRs," Washington, DC, 1982.
[11] T. Yonezawa, K. Onimura, N. Sakamoto, N. Sasaguri, H. Nakata, and H. Susukida, "Effect of Heat Treatment on Stress Corrosion Cracking Resistance of High Nickel Alloys in High Temperature Water," in *Proceedings of the International Symposium on Environmental Degradation of Materials in Nuclear Power Systems-Water Reactors*, 1983, pp. 345–367.
[12] T. Kekkonen, H. Hänninen, The effect of heat treatment on the microstructure and corrosion resistance of inconel X-750 alloy, Corros. Sci. vol. 25 (8–9) (Jan. 1985) 789–803, https://doi.org/10.1016/0010-938X(85)90011-3.
[13] S. Fyfitch, H. Xu, K. Moore, R. Gurdal, and H.T. Tang, "Materials reliability program: PWR internals material aging degradation mechanism screening and threshold values (MRP-175)," Palo Alto, CA, 2005.
[14] J.T.A. Roberts, Metallurgical improvements for enhanced stress corrosion performance of light water reactor structural materials, J. Mater. Energy Syst. vol. 4 (3) (1982) 142–153.
[15] T.R. Mager, "Fastener and bolting material for Westinghouse design internals," in Proceedings: 1986 workshop on advanced high-strength materials, 1989.
[16] S. Hattori, H. Itoh, I. Masaoka, R. Sasaki, R. Watanabe, Stress corrosion cracking of age-hardenable nickel base alloys in high temperature water, Trans. Am. Nucl. Soc. vol. 39 (1981) 451–453.
[17] Gardner G., "Materials reliability program: Pressurized water reactor internals inspection and evaluation guidelines (MRP 227, Revision 2)," 2021.
[18] M.T. Miglin, H.A. Domian, Microstructure and stress corrosion resistance of alloys X750, 718, and A286 in light water reactor environments, J. Mater. Eng. vol. 9 (2) (1987) 113–132.
[19] F.R. Greening, CANDU pressure tube leak detection by annulus gas dew point measurement: a critical review, Kerntechnik vol. 82 (2017) 9–23.
[20] C.D. Judge, "The effects of irradiation on Inconel X-750," McMaster University, Hamilton, ON, 2015.
[21] M. Griffiths *et al.*, "Degradation of Ni-alloy Components in CANDU Reactor Cores," in *AECL-C–127000-CONF-007*, Atomic Energy of Canada Limited, 2013.
[22] M. Wright, "Private communication," *Canadian Nuclear Laboratory - CNL*.
[23] M. Griffiths, The effect of irradiation on Ni-containing components in CANDU® reactor cores: a review, AECL Nucl. Rev. vol. 2 (1) (Jun. 2013) 1–16, https://doi.org/10.12943/ANR.2013.00001.
[24] H.K. Zhang, Z. Yao, C. Judge, M. Griffiths, Microstructural evolution of CANDU spacer material Inconel X-750 under in situ ion irradiation, J. Nucl. Mater. vol. 443 (1–3) (2013) 49–58.
[25] P. Changizian, Z. Yao, C. Lu, F. Long, M.R. Daymond, Radiation effect on nano-indentation properties and deformation mechanisms of a Ni-based superalloy X-750, J. Nucl. Mater. vol. 515 (2019) 1–13.
[26] C.D. Judge *et al.*, "Embrittlement of nickel alloys in a CANDU reactor environment," in *ASTM Special Technical Publication*, 2013, pp. 161–175.
[27] M.N. Tawfeeq, R.J. Klassen, Effect of ion implantation on the grain boundary strength of heat treated Inconel X750, J. Nucl. Mater. vol. 516 (2019) 255–263.
[28] .M. Scott and M.Le Calvar, "Some possible mechanisms of intergranular stress corrosion cracking of alloy 600 in PWR primary water," in Proceedings of the 6th International Symposium on Environmental Degradation of Materials in Nuclear Power Systems-Water Reactors, 1993, pp. 657–667.
[29] G. Bertali, F. Scenini, M.G. Burke, Advanced microstructural characterization of the intergranular oxidation of Alloy 600, Corros. Sci. vol. 100 (2015) 474–483.
[30] G. Bertali, F. Scenini, M.G. Burke, The effect of residual stress on the preferential intergranular oxidation of alloy 600, Corros. Sci. vol. 111 (2016) 494–507, https://doi.org/10.1016/J.CORSCI.2016.05.022.
[31] G. Bertali, F. Scenini, M.G. Burke, The intergranular oxidation susceptibility of thermally–treated Alloy 600, Corros. Sci. vol. 114 (Jan. 2017) 112–122.
[32] L. Volpe, G. Bertali, F. Scenini, M.G. Burke, Effect of temperature on the preferential intergranular oxidation susceptibility of thermally-treated Alloy 600, Corros. Sci. vol. 207 (Oct. 2022) 110565, https://doi.org/10.1016/J.CORSCI.2022.110565.
[33] S.Y. Persaud, A. Korinek, J. Huang, G.A. Botton, R.C. Newman, Internal oxidation of Alloy 600 exposed to hydrogenated steam and the beneficial effects of thermal treatment, Corros. Sci. vol. 86 (Sep. 2014) 108–122, https://doi.org/10.1016/J.CORSCI.2014.04.041.
[34] B. Langelier, S.Y. Persaud, A. Korinek, T. Casagrande, R.C. Newman, G.A. Bottom, Effects of boundary migration and pinning particles on intergranular oxidation revealed by 2D and 3D analytical electron microscopy, Acta Mater. vol. 131 (2017) 280–295.
[35] D.S. Morton, S.A. Attanasio, E. Richey, and G.A. Young, "In search of the true temperature and stress intensity factor dependencies for PWSCC."
[36] G. Economy, R. Jacko, J. Begley, F. Pement, Influence of hydrogen partial pressure on the IGSCC behavior of Alloy 600 tubing in 360 °C water or 400 °C steam, Corrosion vol. 54 (1987).
[37] V.A. Kurepin, D.A. Kulik, A. Hiltpold, and M. Nicolet, "Thermodynamic Modelling of Fe-Cr-Ni-Spinel Formation at the Light-Water Reactor Conditions," Villigen, 2002.
[38] R.A. Robie, B.S. Hemingway, and J.R. Fisher, *Thermodynamic Properties of Minerals and Related Substances at 298.15 K and 1 Bar Pressure and at Higher Temperatures*. Washington: United States Government Printing Office, 1978.
[39] Z. Shen, K. Arioka, S. Lozano-Perez, A study on the diffusion-induced grain boundary migration ahead of stress corrosion cracking crack tips through advanced characterization, Corros. Sci. vol. 183 (2021) 109328.
[40] S.M. Bruemmer, M.J. Olszta, M.B. Toloczko, D.K. Schreiber, Grain boundary selective oxidation and intergranular stress corrosion crack growth of high-purity nickel binary alloys in high-temperature hydrogenated water, Corros. Sci. vol. 131 (2018) 310–323.
[41] L. Volpe, M.G. Burke, F. Scenini, Correlation between grain boundary migration and stress corrosion cracking of alloy 600 in hydrogenated steam, Acta Mater. vol. 186 (Mar. 2020) 454–466, https://doi.org/10.1016/j.actamat.2020.01.020.
[42] L. Volpe, M.G. Burke, F. Scenini, Understanding the role of diffusion induced grain boundary migration on the preferential intergranular oxidation behaviour of Alloy 600 via advanced microstructural characterization, Acta Mater. vol. 175 (Aug. 2019) 238–249, https://doi.org/10.1016/j.actamat.2019.06.021.
[43] S.Y. Persaud, S. Ramamurthy, R.C. Newman, Internal oxidation of alloy 690 in hydrogenated steam, Corros. Sci. vol. 90 (Jan. 2015) 606–613, https://doi.org/10.1016/j.corsci.2014.11.006.
[44] S.Y. Persaud, R.C. Newman, A review of oxidation phenomena in Ni alloys exposed to hydrogenated steam below 500°C," Jul. 01, Natl. Assoc. Corros. Eng. Int. (2016), https://doi.org/10.5006/1957.
[45] G. Economy, R.J. Jacko, F.W. Pement, IGSCC Behavior of Alloy 600 Steam Generator Tubing in Water or Steam Tests Above 360 C, Corrosion vol. 43 (12) (Dec. 1987) 727–734.
[46] L. Volpe, M. Curioni, M.G. Burke, F. Scenini, Thermodynamic equivalence charts for stress corrosion cracking studies in hydrogenated steam, high pressure and supercritical water, J. Electrochem Soc. vol. 168 (1) (Jan. 2021) 011501, https://doi.org/10.1149/1945-7111/abd570.
[47] P.M. Scott, P. Combrade, General corrosion and stress corrosion cracking of Alloy 600 in light water reactor primary coolants, J. Nucl. Mater. vol. 524 (2019) 340–375.
[48] N.S. McIntyre, T.C. Chan, C. Chen, Characterization of oxide structures formed on nickel-chromium alloy during low pressure oxidation at 500 - 600°C, Oxid. Met. vol. 33 (5) (1990) 457–479.
[49] S. Guruswamy, S.M. Park, J.P. Hirth, R.A. Rapp, Internal oxidation of Ag-in alloys: Stress relief and the influence of imposed strain, Oxid. Met. vol. 26 (1) (Aug. 1986) 77–100.
[50] A.E. Yaedu, et al., Preferential intergranular oxidation as a potential degradation mechanism for Alloy X-750CANDU spacers, J. Nucl. Mater. (2024).
[51] F. Scenini, R.C. Newman, R.A. Cottis, R.J. Jacko, Effect of surface preparation on intergranular stress corrosion cracking of alloy 600 in hydrogenated steam, Corrosion vol. 64 (11) (Nov. 2008) 824–835, https://doi.org/10.5006/1.3279916.
[52] L. Chang, M.G. Burke, F. Scenini, Stress corrosion crack initiation in machined type 316L austenitic stainless steel in simulated pressurized water reactor primary water, Corros. Sci. vol. 138 (2018) 54–65.
[53] F. Scenini and R.C. Newman, "Alloy oxidation studies related to PWSCC," in Proceedings of the 12th International Conference on Environmental Degradation of Materials in Nuclear Power Systems-Water Reactors, 2005, pp. 891–902.
[54] M. Burke, T. Mager, and I. Wilson, "The effect of cooling rate on precipitate morphology in Alloy X-750," in Proceedings of the fifth international symposium on environmental degradation of materials in nuclear power systems - water reactors, 1992, pp. 287–293.
[55] K. Hosoi, S. Hattori, I. Masaoka, and R. Sasaki, "Relation between susceptibility to stress corrosion cracking in high temperature water and microstructure of Inconel Alloy X-750," in Proceedings of the International Symposium on Environmental Degradation of Materials in Nuclear Power Systems - Water Reactors, Myrtle Beach, 1983, pp. 334–344.
[56] R.W. Balluffi, J.W. Cahn, Mechanism for diffusion induced grain boundary migration, Acta Metall. vol. 29 (3) (1981) 493–500.

[57] T.D. Nguyen, J. Zhang, D.J. Zhang, Effects of Si, Al and Ti on corrosion of Ni-20Cr and Ni-30Cr alloys in Ar- 20CO2-20H2O gas at 700 °C, Corros. Sci. vol. 170 (2020) 108702.
[58] P. Kofstad, High Temperature Oxidation of Metals, John Wiley & Sons, New York, NY, 1966.
[59] F.H. Stott, G.C. Wood, Internal oxidation, Mater. Sci. Technol. vol. 4 (12) (Dec. 1988) 1072–1078, https://doi.org/10.1179/mst.1988.4.12.1072.
[60] G.C. Wood, F.H. Stott, D.P. Whittle, Y. Shida, B.D. Bastow, The high-temperature internal oxidation and intergranular oxidation of nickel-chromium alloys, Corros. Sci. vol. 23 (1) (Jan. 1983) 9–25, https://doi.org/10.1016/0010-938X(83)90056-2.
[61] G.P. Sabol, R. Stickler, Microstructure of nickel-based superalloys, Phys. Status Solidi (b) vol. 35 (1) (1969) 11–52.
[62] S.Y. Persaud et al., "Grain boundary embrittlement of alloy 600 by internal oxidation in simulated primary water environments," in 16th International Conference on Environment Degradation of Materials in Nuclear Power Systems—Water Reacter, 2013.
[63] B. Lewis, G. Von Elbe, Combustion, flames and explosions of gases, 3rd ed. Academic Press, 1987.
[64] A. Riahi, H. Zhu, A. Eskandari, S.Y. Persaud, R.C. Newman, New insights into internal oxidation of alloy 690 and model alloys in hydrogenated steam, Corrosion vol. 4439 (2023).
[65] S.M. Bruemmer, G.S. Was, Microstructural and microchemical mechanisms controlling intergranular stress corrosion cracking in light-water-reactor systems, J. Nucl. Mater. vol. 216 (1994) 348–363.
[66] T.R. Mager, I.L.W. Wilson, and J.L. Nelson, "Improved stress corrosion resistance of NiCrFe alloys," Palo Alto, CA, 1990.
[67] W. Lunceford, T. DeWees, P. Scott, and T. Lian, "EPRI Materials Degradation Matrix, Revision 3," Palo Alto, CA, 2013.
[68] H.A. Domian, D.L. Baty, and J.L. Nelson, "Microstructure and stress corrosion resistance of alloys X-750, 718, and A-286 in LWR Environments," 1989, *EPRI NP-6392SD, Palo Alto, CA*.
[69] S. Cruchley, H.E. Evans, M.P. Taylor, M.C. Hardy, S. Stekovic, Chromia layer growth on a Ni-based superalloy: sub-parabolic kinetics and the role of titanium, Corros. Sci. vol. 75 (2013) 58–66.
[70] H.J.T. Ellingham, Reducibility of oxides and sulphides in metallurgical processes, J. Soc. Chem. Ind. vol. 5 (1944) 125–133.
[71] F.H. Stott, G.C. Wood, J. Stringer, The influence of alloying elements on the development and maintenance of protective scales, Oxid. Met. vol. 44 (1995) 113–145.
[72] D.J. Young, *High temperature oxidation and corrosion of metals*, 1st ed. Amsterdam, Elsevier, 2016.
[73] M. Birks, G.H. Meier. Introduction High Temperature Oxidation Metals, second ed, Cambridge University Press, 2006.
[74] Y. Ghaffari, K. Daub, F. Long, S.Y. Persaud, Intergranular oxidation behaviour of Ni-Cr-Al model alloys in 480 °C hydrogenated steam, Corros. Sci. vol. 226 (2024) 111678.
[75] Y. Ghaffari, K. Daub, F. Long, M. Topping, S. Persaud, Comparing the intergranular oxidation of Ni-Cr and Ni-Al model alloys in 480 °C hydrogenated steam, Scr. Mater. vol. 232 (2023) 115501, https://doi.org/10.1016/j.scriptamat.2023.115501.
[76] F.H. Stott, F.I. Wei, High temperature oxidation of commercial austenitic stainless steels, Mater. Sci. Technol. vol. 5 (1989) 1140–1147.
[77] H. Nagai, M. Okabayashi, H. Mitani, The effects of rare earths and reactive elements on the oxidation resistance of Ni-20Cr alloy, Trans. Jpn. Inst. Met. vol. 21 (1980) 341–348.
[78] J.H. Chen, P.M. Rogers, J.A. Little, Oxidation behavior of several chromia-forming commercial nickel-base superalloys, Oxid. Met. vol. 47 (1997) 381–410.
[79] D. Kim, C. Jang, W.S. Ryu, Oxidation characteristics and oxide layer evolution of Alloy 617 and Haynes 230 at 900 °C and 1100 °C, Oxid. Met. vol. 71 (2009) 271–293.
[80] B. Gleeson, High-Temperature Corrosion of Metallic Alloys and Coatings, in: R. W. Cahn, P. Haasen, E.J. Kramer (Eds.), Corrosion and Environmental Degradation, vol. 1, WILEY-VCH, Weinheim, 2000.